TU Delft

Delft University of Technology

Document Version
Final published version

Licence
CC BY

Citation (APA)
Gutierrez-Santiago, U., Keller, J., Fernández-Sisón, A., Polinder, H., & van Wingerden, J. W. (2025). Field validation of dynamic mechanical torque measurements using fiber-optic strain sensors for geared wind turbines. *Forschung im Ingenieurwesen/Engineering Research*, *89*(1), Article 45. https://doi.org/10.1007/s10010-025-00793-3

Important note
To cite this publication, please use the final published version (if applicable).
Please check the document version above.

Copyright
In case the licence states “Dutch Copyright Act (Article 25fa)”, this publication was made available Green Open Access via the TU Delft Institutional Repository pursuant to Dutch Copyright Act (Article 25fa, the Taverne amendment). This provision does not affect copyright ownership.
Unless copyright is transferred by contract or statute, it remains with the copyright holder.

Sharing and reuse
Other than for strictly personal use, it is not permitted to download, forward or distribute the text or part of it, without the consent of the author(s) and/or copyright holder(s), unless the work is under an open content license such as Creative Commons.

Takedown policy
Please contact us and provide details if you believe this document breaches copyrights.
We will remove access to the work immediately and investigate your claim.

This work is downloaded from Delft University of Technology.

Forschung im Ingenieurwesen (2025)89:45
https://doi.org/10.1007/s10010-025-00793-3

ORIGINALARBEITEN/ORIGINALS

Field validation of dynamic mechanical torque measurements using fiber-optic strain sensors for geared wind turbines

Unai Gutierrez-Santiago[1,2] · Jonathan Keller[3] · Alfredo Fernández-Sisón[2] · Henk Polinder[1] · Jan-Willem van Wingerden[1]

Received: 15 September 2024 / Accepted: 30 January 2025
© The Author(s) 2025

Abstract

Accurate knowledge of the mechanical loads of wind turbine gearboxes has become essential in modern, highly loaded gearbox designs, as maintaining or even improving gearbox reliability with increasing torque density demands is proving to be challenging. Unfortunately, the traditional method of measuring dynamic mechanical torque using strain gauges placed on the outer surface of a rotating shaft and transmitting the resulting signal is unsuitable for serial deployment due to technical and economic constraints. An alternative method based on fiber-optic strain sensors placed on the stationary outer surface of the gearbox ring gear has been proposed. Like shaft torsion, the radial deformation of the ring gear is proportionate to the rotor torque. Placing the sensors on a stationary component is a cost-effective alternative for serial implementation because the need for complex and expensive data transfer via wireless transmission or a slip ring is eliminated. In this paper, we present the results of an extensive field experiment conducted to evaluate the torque measurement accuracy of this novel sensing solution installed on the gearbox of a Gamesa G97 2-MW wind turbine at the National Renewable Energy Laboratory's Flatirons Campus. Torque measurements derived from fiber-optic strain sensors placed on the ring gear of the planetary stage are compared to conventional torque measurements from strain gauges placed on the main shaft. Two different torque estimation data processing methods were evaluated, with the method based on operational deflection shapes providing the most accurate results with an average normalized root mean square error below 0.7% for a load revolution distribution analysis. The effect of operating conditions on the torque estimate was also investigated, and the third planet-passing operational deflection shape was found to be the least sensitive to nontorque load-related effects. The fiber-optic strain sensors' successful operation during the complete test campaign has demonstrated a robust and accurate solution for fleet-wide enhanced gearbox remaining useful life estimation.

Jonathan Keller, Alfredo Fernández-Sisón, Henk Polinder and Jan-Willem van Wingerden contributed equally to this work.

✉ Unai Gutierrez-Santiago
u.gutierrezsantiago@tudelft.nl

Jonathan Keller
jonathan.keller@nrel.gov

Alfredo Fernández-Sisón
alfredo.fernandez.s@siemensgamesa.com

Henk Polinder
h.polinder@tudelft.nl

Jan-Willem van Wingerden
j.w.vanwingerden@tudelft.nl

[1] TU Delft 3mE, Mekelweg 2, 2628 CD Delft, The Netherlands

[2] Siemens Gamesa Renewable Energy, Parque Tecnológico de Bizkaia, 48170 Zamudio, Spain

[3] National Renewable Energy Laboratory, Denver West Parkway, Golden, CO 15013, USA

Published online: 03 March 2025

Feldvalidierung dynamisch-mechanischer Drehmomentmessungen mittels faseroptischer Dehnungssensoren für Windkraftanlagen mit Getriebe

Zusammenfassung

Genaue Kenntnisse über die mechanischen Belastungen von Windkraftanlagengetrieben sind bei modernen, hochbelasteten Getriebekonstruktionen unverzichtbar geworden, da sich die Aufrechterhaltung oder sogar Verbesserung der Getriebezuverlässigkeit bei steigenden Anforderungen an die Drehmomentdichte als Herausforderung erweist. Leider ist die herkömmliche Methode zur Messung des dynamischen mechanischen Drehmoments mithilfe von Dehnungsmessstreifen, die auf der Außenfläche einer rotierenden Welle angebracht sind und das resultierende Signal übertragen, aufgrund technischer und wirtschaftlicher Einschränkungen für den Serieneinsatz ungeeignet. Es wurde eine alternative Methode vorgeschlagen, die auf faseroptischen Dehnungssensoren basiert, die auf der stationären Außenfläche des Getriebezahnkranzes angebracht sind. Wie die Wellentorsion ist die radiale Verformung des Zahnkranzes proportional zum Rotordrehmoment. Die Platzierung der Sensoren auf einem stationären Bauteil ist eine kostengünstige Alternative für die Serienimplementierung, da die Notwendigkeit einer komplexen und teuren Datenübertragung über eine drahtlose Übertragung oder einen Schleifring entfällt. In diesem Artikel präsentieren wir die Ergebnisse eines umfangreichen Feldversuchs, der durchgeführt wurde, um die Drehmomentmessgenauigkeit dieser neuartigen Sensorlösung zu bewerten, die auf dem Getriebe einer 2-MW-Windkraftanlage Gamesa G97 auf dem Flatirons Campus des National Renewable Energy Laboratory installiert ist. Drehmomentmessungen, die von faseroptischen Dehnungssensoren am Hohlrad der Planetenstufe abgeleitet werden, werden mit herkömmlichen Drehmomentmessungen von Dehnungsmessstreifen an der Hauptwelle verglichen. Es wurden zwei verschiedene Datenverarbeitungsmethoden zur Drehmomentschätzung ausgewertet, wobei die Methode auf der Grundlage von Betriebsschwingformen die genauesten Ergebnisse mit einem durchschnittlichen normalisierten quadratischen Mittelwertfehler von unter 0,7 % für eine Lastumdrehungsverteilungsanalyse lieferte. Die Auswirkungen der Betriebsbedingungen auf die Drehmomentschätzung wurden ebenfalls untersucht, und die dritte Betriebsschwingform beim Planetendurchgang erwies sich als am wenigsten empfindlich gegenüber nicht drehmomentbezogenen Lasteffekten. Der erfolgreiche Betrieb der faseroptischen Dehnungssensoren während der gesamten Testkampagne hat eine robuste und genaue Lösung für eine verbesserte Schätzung der verbleibenden Nutzungsdauer von Getrieben in der gesamten Flotte gezeigt.

1 Introduction

Wind turbine power ratings, rotor diameters, and hub heights have grown significantly to reduce the cost of wind energy [1]. The wind turbine drivetrain converts mechanical power to electrical power and transmits the rotor loads to the bedplate and tower [2]; it makes an appreciable contribution to the capital expenditure of the turbine [3]. Many wind turbine drivetrains use gearboxes to lower the capital cost of the drivetrain, but its reliability is essential and remains a top priority because gearbox failures cause long downtime with costly repairs and contribute appreciably to the turbine operation and maintenance costs [4–6]. Thanks to internationally recognized gearbox wind turbine design standards like IEC 61400-4 and AGMA 6006 and collaborative efforts like the Drivetrain Reliability Collaborative between turbine manufacturers, gearbox designers, bearing suppliers, and research institutions like the National Renewable Energy Laboratory (NREL) and Argonne National Laboratory, average annual gearbox failure rates for the U.S. land-based fleet have dropped from 5% to 10% 20 years ago [7] to 2.5% more recently [8]. Yet, there is room for improvement because gearboxes still generally do not reach their desired design life [9]. These standards have placed greater rigor on the design and gearbox verification process, including the effects of rotor nontorque loads [10], transient events [11, 12], and electrical currents [13]. However, the rapid pace at which torque density requirements have risen has led to increasingly complex and lightweight designs with new reliability challenges and additional requirements, such as complying with stricter noise demands and more prominent dynamic interactions.

Accurate knowledge of the dynamic mechanical torque in wind turbine gearboxes is essential to complying with these requirements and improving their reliability. Dynamic mechanical torque measurements of every gearbox in a fleet can enhance drivetrain usage monitoring because the consumed fatigue life can be assessed more precisely using the measured torque values throughout their entire commercial operation. Dynamic torque measurements can also potentially be used by the wind turbine controller for improved wind turbine control to achieve a reduction of torque oscillations (i.e., torsional damping). Additionally, dynamic mechanical torque measurements can be used to quantify drivetrain efficiency. Unfortunately, sensors that provide detailed load measurements of the turbine during commercial operation are not generally available [14]. It is possible to estimate the mechanical gearbox torque from the electric currents in the generator, but this requires assumptions about the variable gearbox, generator, and power converter

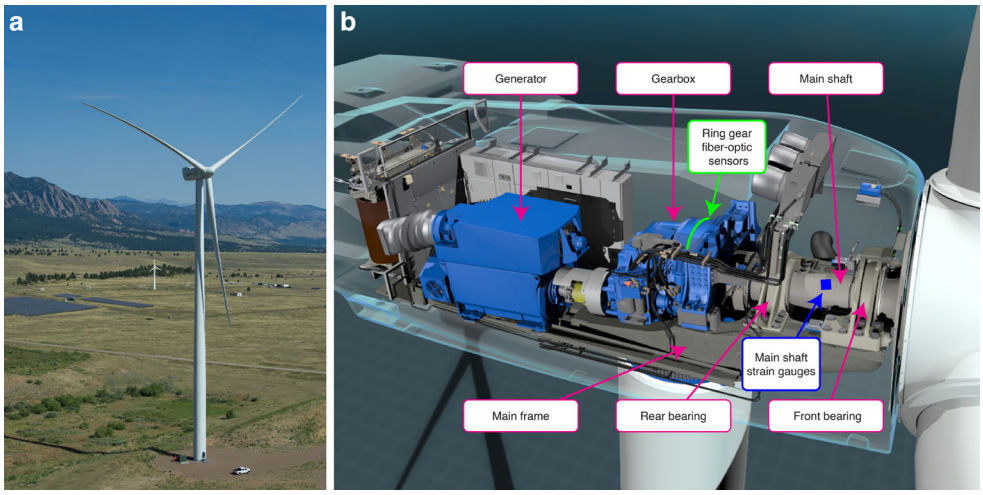


Fig. 1 **a** G97 2 MW wind turbine on NREL's Flatirons Campus; photo from Dennis Schroeder, NREL 21886. **b** Nacelle schematic (source Nextwave Multimedia https://www.nextwavemultimedia.com/blog/3d-animation/this-time-a-stereoscopic-3d-av-for-gamesa-by-nextwave/)

efficiencies for fatigue life calculations and is not available for estimation of the severity of high-load, damaging events like emergency braking and low-voltage ride through when the generator disconnects from the grid [12, 15–17]. The conventional method to measure dynamic mechanical torque is based on bonding strain gauges to a rotating drive shaft. The strain gauges convert the torsional deformation caused by the torque into a change in electrical resistance. Transferring the resulting signal from the rotating shaft to a stationary data logging system and powering the data acquisition devices is difficult and costly. In wind turbines, the main shaft's torsional deformation is also small because of its high stiffness, which typically results in a low signal-to-noise ratio. The torsional deformation of the gearbox output shaft is higher, but accessing this shaft can require special provisions [12]. These drawbacks have limited the use of such measurements to laboratory environments [10], validation and certification of experimental wind turbines [18], and troubleshooting exercises [19]. Other researchers have focused on indirect techniques or so-called virtual sensors where a model of the system is combined with data from sensors in other locations of the turbine to obtain an estimate of dynamic mechanical torque [20–26].

Installation of fiber-optic sensors (FOSs) in other wind turbine components, such as blades [27], has recently become more common. FOSs offer several advantages compared to traditional electrically resistive strain gauges, including higher signal-to-noise ratio, immunity to electromagnetic interference, and the ability to accommodate many strain sensors in a single fiber [28]. Previous work demonstrated an alternative method to measure the dynamic mechanical torque based on deformation measurements of the static first-stage ring gear using fiber-optic strain sensors during a bench test of a 6 MW wind turbine gearbox with 5 planets [29]. By measuring strain on the static or fixed frame, the difficulties related to data transfer from a rotating shaft and the power supply of the electronic components on the shaft are avoided. However, this work was conducted on a back-to-back gearbox test bench intended for validation and certification of new gearbox designs and for end-of-line testing of serial production units. Such test benches typically have limited capabilities for producing dynamic torque and generally cannot create controlled nontorque

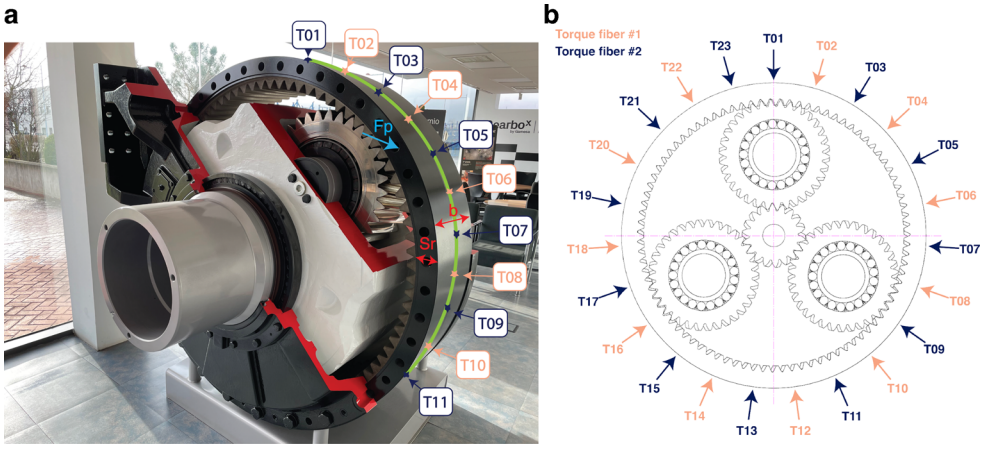


Fig. 2 G97 2 MW gearbox with **a** representation of fiber-optic strain sensors on the outer surface of the first stage ring gear installed for torque measurements (adaptation of figure from Gamesa Gearbox) (https://www.gamesagearbox.com/wind-technology/) and **b** angular placement of the 23 FBGs labeled T01 to T23, with the 12 sensors in blue belonging to fiber number one, and the 11 sensors in red to fiber number two

loads, such as axial loads and bending moments created by the rotor. Field testing provides the most realistic platform for performance evaluation of this fiber-optic-based torque measurement method, as certain problems related to the interaction of multiple drivetrain components can only be discovered after deployment in the field [30].

In the work described in this paper, we took the next step in technology development and validation of dynamic mechanical torque measurements using fiber-optic strain sensors by:

- Conducting an extensive field validation campaign to demonstrate the use of FOSs for wind turbine gearbox dynamic mechanical torque measurements, contributing to an increase in the technology readiness level from 6 to 7 as defined in ISO 16290.
- Assessing the accuracy of dynamic mechanical torque measurements by comparing the results gathered from fiber-optic strain sensors to reference torque measurements from conventional strain gauges installed on the main shaft over a wide range of normal power production conditions.
- Investigating the effects of wind turbine operating conditions on the quality of dynamic mechanical torque measurements, with a special focus on the effects produced by nontorque loads and ring gear temperature.

The remainder of the paper is structured as follows. In Sect. 2, we describe the measurement setup and test program. In Sect. 3, two alternative data processing procedures are described to derive gearbox torque from fiber-optic strain signals. In Sect. 4, the key findings from the validation campaign are described, and finally, Sect. 5 summarizes the main conclusions of this work.

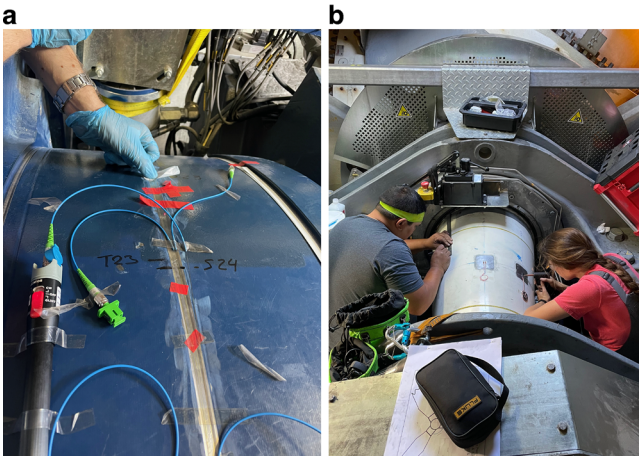


Fig. 3 Torque measurements from **a** ring gear FBGs and **b** main-shaft strain gauges. Photos from Unai Gutierrez-Santiago, Siemens Gamesa Renewable Energy, NREL 85910 and 91649

2 Experimental setup

The present study was conducted on a Gamesa G97 2 MW wind turbine located at the NREL Flatirons Campus (Colorado, USA) as shown in Fig. 1a. The G97 turbine has a four-point mount drivetrain, in which two spherical roller bearings 1.3 m apart support the main shaft and transfer all rotor nontorque loads to the main frame. The main shaft then transmits nearly only torque to the gearbox planet carrier. The gearbox planetary stage includes three equally spaced planets meshing with the ring gear and a floating sun pinion, while two additional parallel stages use helical gearing. The gearbox provides a total gear ratio of 126.328, which at a rated rotor speed of 15.96 rpm results in a speed of 2,016 rpm of the doubly-fed induction generator. The gearbox mass is 14,620 kg, resulting in a torque density of 90 Nm/kg at a reference (rated) mechanical torque of 1,320 kNm. This torque density was quite common at the time of development of the G97, but modern gearboxes are now being produced with torque densities over 200 Nm/kg [2, 29]. During the test campaign, data were collected from three different sources [31]:

1. FOSs installed on the outer surface of the gearbox ring gear to measure ring gear deformation
2. Meteorological and drivetrain sensors to measure rotor inflow conditions and main-shaft loads
3. Wind turbine operational parameters collected from the turbine controller.

An overview of the drivetrain arrangement with the location of the gearbox ring gear FOSs and the main-shaft strain gauges are also shown in Fig. 1b.

2.1 Ring gear fiber-optic sensors

Two fibers with a total of 23 FOSs were installed around the outer surface of the ring gear of the gearbox at the midpoint of the ring gear face width. Figure 2a shows the planetary stage of a G97 gearbox as seen from the rotor side. The sensors were located at the midpoint of the ring gear width, b, and evenly distributed around the ring gear circumference as shown in Fig. 2b. In operation, the mesh force between the planets and ring gear, F_p, causes deformation of the ring gear proportionate to the rotor torque as the planets orbit around the ring gear. Because the ring gear rim thickness, S_r, is relatively thin, significant deformations can be measured by FOSs well within their sensing capabilities [29]. The FOSs used for the present study are based on Fiber Bragg Gratings (FBGs) and are commonly classified as discrete sensors. FBGs are modifications to the fiber's core in discrete, short segments that reflect particular wavelengths of light and transmit all others. FBGs are used extensively for sensing applications because the reflected wavelength

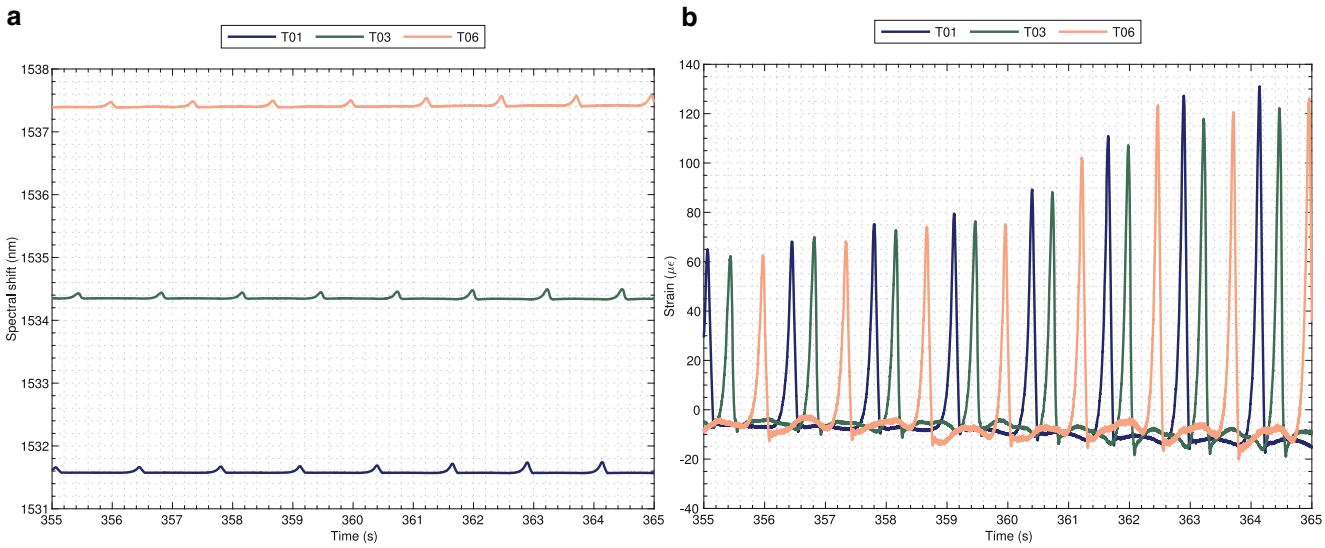


Fig. 4 Example fiber-optic response for sensors T01, T03, and T06: **a** raw spectral shift and **b** resulting filtered strain

is sensitive to temperature and strain changes at the grating and offer several advantages compared to electrical strain gauges [28]. FBGs offer a higher signal-to-noise ratio than strain gauges and are immune to electromagnetic interference. A single optical fiber can also accommodate multiple sensors, simplifying the installation process. For torque measurement, a total of 23 FBGs was chosen because it is a noninteger multiple of the three planets, in contrast with the 24 FBGs that were intentionally chosen as an integer multiple of the three planets for previous planet load-sharing measurements [31]. The FBGs for torque measurement were accommodated in two optical fibers, with 11 and 12 FBGs. In Fig. 2b, the sensors have been color-coded depending on the optical fiber to which they belong. The fibers were bonded with cyanoacrylate glue to the outer surface of the ring gear in an existing machined groove. A snapshot of the uptower installation process is shown in Fig. 3a. Because the sensors were retrofitted to an operational wind turbine, the protective paint on the ring gear had to be removed by sanding to allow for better bonding between the fibers and the ring. In operation, an interrogator sends light into the fibers and analyzes the wavelengths reflected by the gratings. The interrogator extracts a signal proportional to the spectral shift in each FBG caused by mechanical and thermal strain. The interrogator used for the measurement campaign provided a sampling frequency of 2,000 Hz for each signal. Sensing360 B.V. supplied the FOSs and the interrogator.

2.2 Meteorological and drivetrain sensors

A second set of sensors were installed on a meteorological tower in front of the wind turbine and the drivetrain to gather related operational data for comparison to and

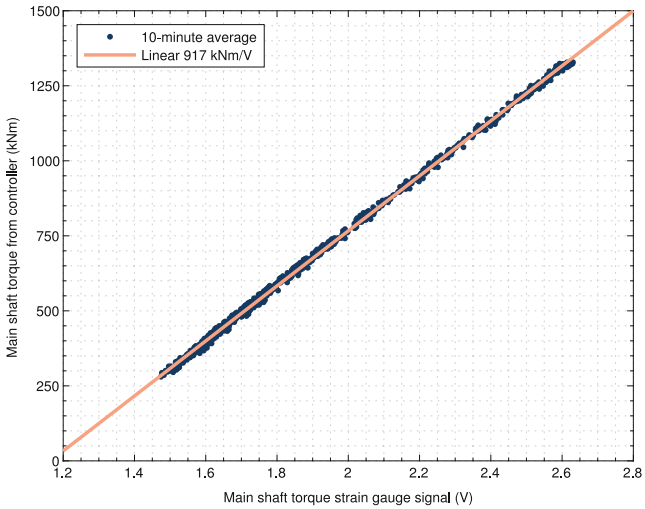


Fig. 5 Linear interpolation between main-shaft strain gauge response and mechanical torque derived from turbine controller using 10-minute average values from April 25th to July 20th

analysis of the fiber-optic measurements. The inflow wind conditions were gathered from the NREL M4/site 4.4 meteorological tower located near the wind turbine. Wind speed, wind direction, and temperature measurements at hub height were recorded. For the drivetrain, three full Wheatstone bridges consisting of weldable strain gauges were placed on the outer surface of the tapered main shaft at a diameter of 553 mm and approximately halfway between the two main bearings, 2.29 m from the rotor center of gravity and 0.62 m from the front main bearing as shown in Fig. 3b. LEA-06-W125F-350/3R strain gauges were used to measure the main-shaft torque and LEA-06-W250B-350 strain gauges were used to measure the two orthogonal main-shaft bending moments. A battery-pow-

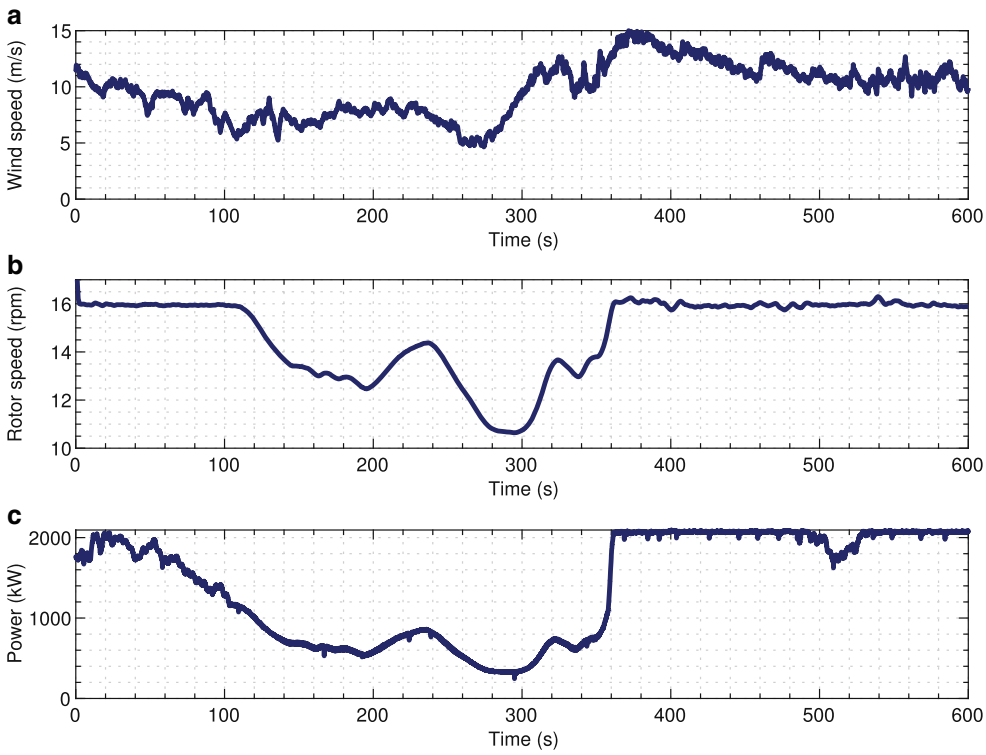


Fig. 6 Wind speed at hub height, rotor speed, and total produced power recorded for the example 10-minute period of turbine operation on April 25th beginning at 20:40 UTC

ered V-Link transmitter system was used to transmit the bridge outputs to a base station where they were recorded in units of volts. A CEV58M-1600 absolute rotary shaft encoder was installed to measure absolute azimuth angle to relate both the fiber-optic strains measured on the static ring gear described in the previous section and the main-shaft strains to the angular position of the main shaft and rotor. A zero-degree azimuth angle was set referenced to the blade labeled as "A" when pointing down. Additionally, an SA1 resistance temperature detector was installed on the outer surface of the bottom of the ring gear to measure its temperature and assess the effect of thermally induced strains in the FBGs on the accuracy of the torque measurements. These data were recorded by an NREL-operated, GPS-time-synchronized, National Instruments-based EtherCAT data acquisition system at a sampling rate of 60 Hz for 10-minute periods.

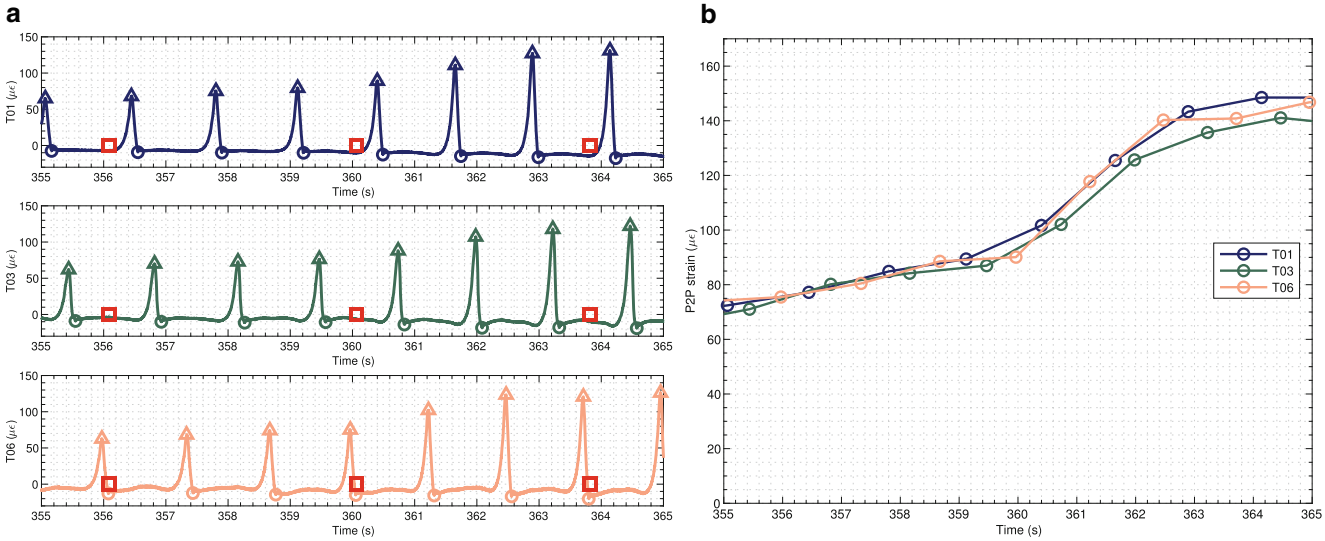


Fig. 7 Example P2P strain processing for sensors T01, T03, and T06: **a** P2P identification and **b** P2P strain magnitude

2.3 Turbine operation parameters

The last data source was the turbine controller. Using a proprietary data acquisition system supplied by Siemens Gamesa, several operational parameters were recorded with a sampling frequency of 25 Hz. These operational parameters included the wind speed measured by the turbine, nacelle direction, total power produced, generator and rotor speed, gearbox oil sump and high-speed shaft bearing temperature, nacelle and exterior temperature, pitch angles, and pitch angle rates.

2.4 Test program

The measurement and data acquisition equipment were active from April 25th to July 20th, 2023. During this period, the turbine was operated using the standard controller parameters to reproduce normal working conditions. The acquired data described in Sect. 2.1 to 2.3 were then post-processed and binned together into 10-minute files for ease of handling and analysis. All three data acquisition systems were synchronized using the Coordinated Universal Time (UTC) timestamp, verified by comparing the rotor speed recorded by the controller versus the rotor speed as calculated from the main-shaft azimuth encoder and FOSs. In total, 837 10-minute files were recorded with all data acquisition systems operational and with a minimum of 150 kW, 238 of which were above 50% rated torque. The wide range of operating conditions experienced during the test campaign covered the complete power curve of the turbine [31].

2.5 Filtering of fiber-optic sensor signals and conversion to strain

Figure 4a shows the raw spectral shift recorded by the interrogator for sensors T01, T03, and T06 during an example 10-second portion on April 25th beginning at 20:45:55 UTC. The moving average was subtracted from the raw spectral shift to remove the specific spectral offset and thermally induced strain from each FOS. The remaining filtered signal is assumed to be produced by only the planet passage effect and can then be converted to strain using a linear conversion factor of 840.34 $\mu\epsilon$/nm as shown in Fig. 4b.

2.6 Calibration of torque measurement with main-shaft strain gauges

The 10-minute average of the main-shaft Wheatstone torque bridge was calibrated through a linear regression to the estimated rotor mechanical torque derived from the turbine operation parameters for all datasets with a minimum value of 150 kW of total power production. Because the strain gauges were installed *in situ* uptower, the measured strain was correlated to the main-shaft mechanical torque estimated from the power managed by the turbine controller and rotor speed measurements along with an assumed factor of 1.1 to account for typical power converter, generator, and gearbox efficiency losses. For the purposes of this work, such a reference torque is sufficient to compare the relative accuracies of the different methods used to determine torque from the FOSs. Figure 5 shows the resulting correlation. As expected, a linear relationship was found with an interpolation coefficient of 917 kNm/V. The main-shaft bending measurements were also calibrated by relating the response from the corresponding Wheatstone bridges in turbine idling conditions to the expected bending moment of 395 kNm at the Wheatstone bridge location, which was derived from a force balance of the drivetrain subject to the approximate rotor mass of 34,000 kg and the counterbalancing effect of the gearbox mass. In this calculation, the drivetrain tilt angle of 6 degrees was also accounted for and the spherical main bearings were assumed to support only radial and/or axial loads, but not any moments [32]. These methods are common in field testing of installed wind turbines [18].

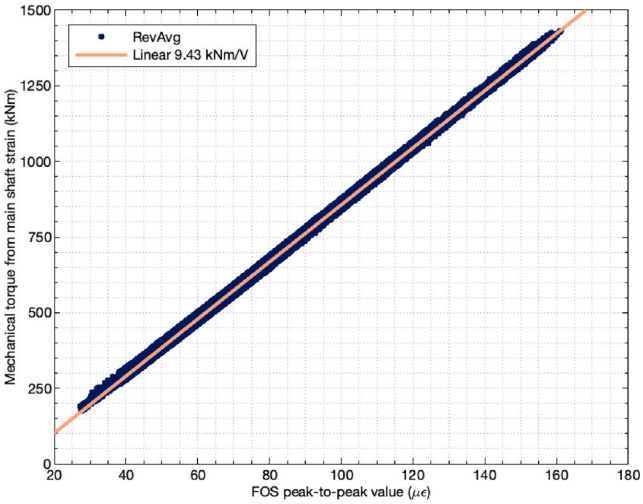


Fig. 8 Linear interpolation between nP2P values and main-shaft mechanical torque using main-shaft revolution average values from April 25th to July 20th

3 Measuring dynamic mechanical torque with ring gear fiber-optic sensors

This section describes how the strain signals from the fiber-optic sensors placed on the outer surface of the ring gear are processed to derive the dynamic mechanical torque applied to the gearbox. Two alternatives to derive torque from strain are examined using an example 10-minute period of turbine operation on April 25th beginning at 20:40 UTC. The wind

Table 1 ODS frequencies in rated conditions identified by the MOESP algorithm using $s = 64$ and $n = 20$

Mode	Frequency (Hz)	3P Order	Damping ratio	Acronym
1	0.80	1.00	2.15e-5	3P
2	1.60	2.00	1.24e-5	2×3P
3	2.39	3.00	1.16e-5	3×3P
4	3.19	4.00	1.10e-5	4×3P
5	3.99	5.00	9.29e-5	5×3P
6	4.78	6.00	1.26e-5	6×3P
7	5.58	6.99	1.34e-5	7×3P
8	6.38	7.99	1.30e-5	8×3P
9	7.18	8.99	1.86e-5	9×3P
10	7.97	9.99	3.91e-5	10×3P

speed at hub height, the rotor speed, and the total produced power during this 10-minute period are shown in Fig. 6. For the first 2 min, the wind speed was just under the rated wind speed of 11 m/s, so the turbine was operating the rated rotor speed of 15.96 rpm, but slightly less than the rated power of 2 MW. During the next 4 min the wind speed dropped to as low as 5 m/s, so the turbine operated with variable rotor speed and power as low as 300 kW. For the last 4 min, the wind speed increased quickly to as high as 15 m/s, so the turbine operated largely at rated rotor speed and torque.

3.1 Peak-to-peak method

This section describes how the fiber-optic strain data were processed to obtain a torque estimate based on the change of the peak-to-peak (P2P) strain values over time [29]. Once signals have been filtered as described in Sect. 2.5, the remaining signal is assumed to be entirely caused by strain at the FBG as shown in Fig. 4b. The signals of all 23 sensors exhibit large tensile strain peaks followed by a compressive peak as each of the three planet gears passes the sensor, which occurs three times per-rotor revolution (3P). Figure 7a shows the identified tensile and compressive peaks of sensors T01, T03, and T06 over a 5-second portion of the example, during which each sensor witnessed 8 planet passes. The red squares depict the moment when the main-shaft azimuth angle equaled zero, signaling a complete revolution of the rotor. Figure 7b shows the resulting P2P values for the same period. The P2P strains measured at each sensor location are slightly different in magnitude and occur at slightly different times. Several factors are expected to play a role in the observed differences in the torque-to-deformation relationship. Although the ring gear itself is axisymmetric as shown in Fig. 2b, the front and rear housings connected to the ring gear and especially the torque reaction arms are not as shown in Fig. 1b and thus result in a nonuniform stiffness for the complete system. Because there are 23 sensors and 87 ring gear teeth, the sensors each have different circumferential positions relative to the ring gear teeth. If the distribution of load over the teeth is not exactly the same, it can result in slightly different strain at each sensor location. Finally, the bonding between the fiber and the ring gear is a manual process that could lead to differences in sensitivity to strain of each sensor, especially for this *in situ* installation.

Although torque can be estimated from the P2P strain of just a single FOS, doing so would only result in a torque measurement at the time of each planet passage at a frequency of 3P. Combining the P2P strain for all the sensors around the ring gear circumference into a single measure would result in a torque measurement at a much higher frequency of 23 times 3P; however, the identified minor differences in strain for each sensor must be accounted for. In this work, the average P2P value of each sensor was used to normalize and combine the P2P strains into a single measure. Like the main-shaft strain gauges, the FOSs could not

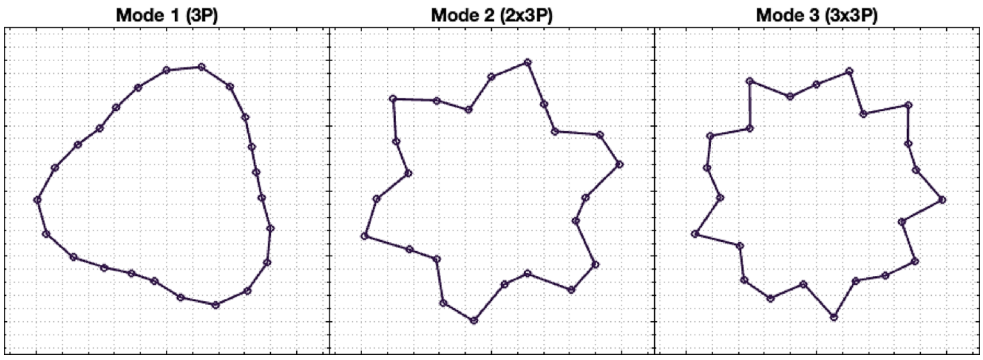


Fig. 9 Simulated strains on the ring gear associated with the first three planet-passing mode shapes

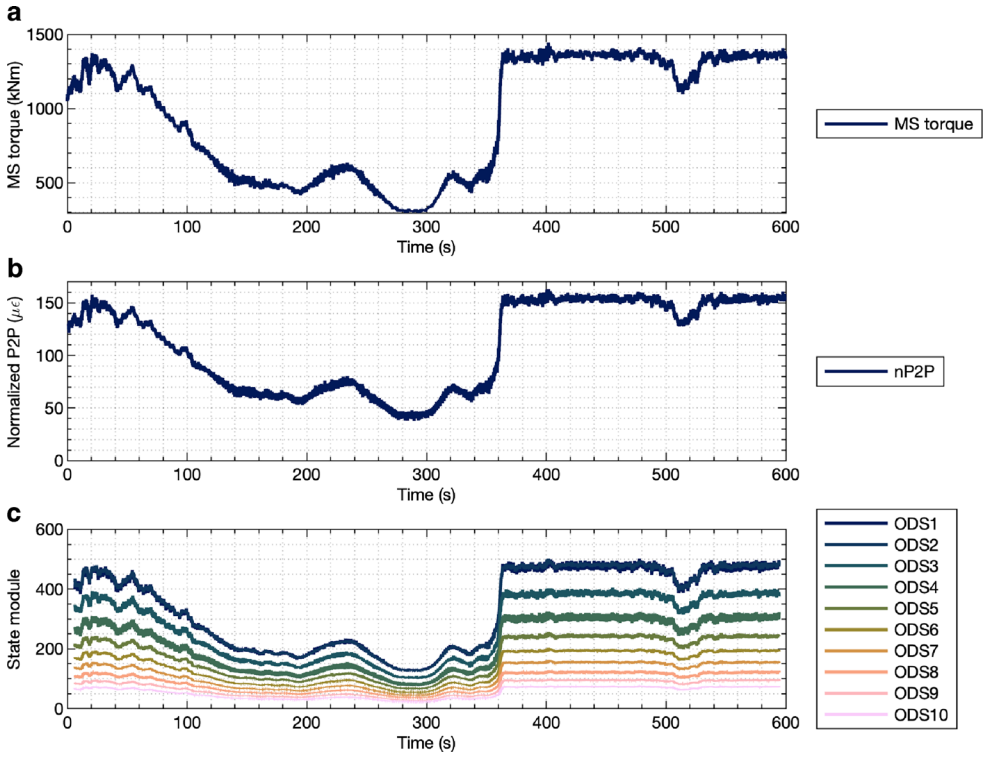


Fig. 10 Evolution of the module of each state associated with the identified ODSs for the 10-min recording from April 25th at 20:40 UTC

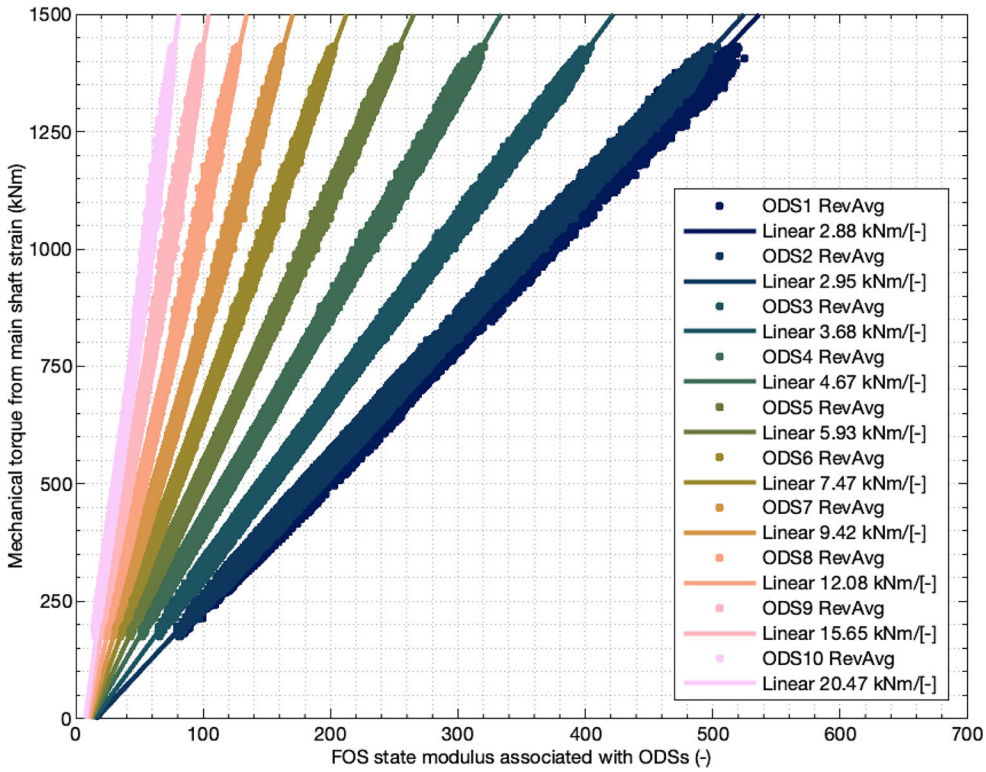


Fig. 11 Linear interpolation between modules of reconstructed states for each ODS and main-shaft mechanical torque using main-shaft revolution average values from April 25th to July 20th

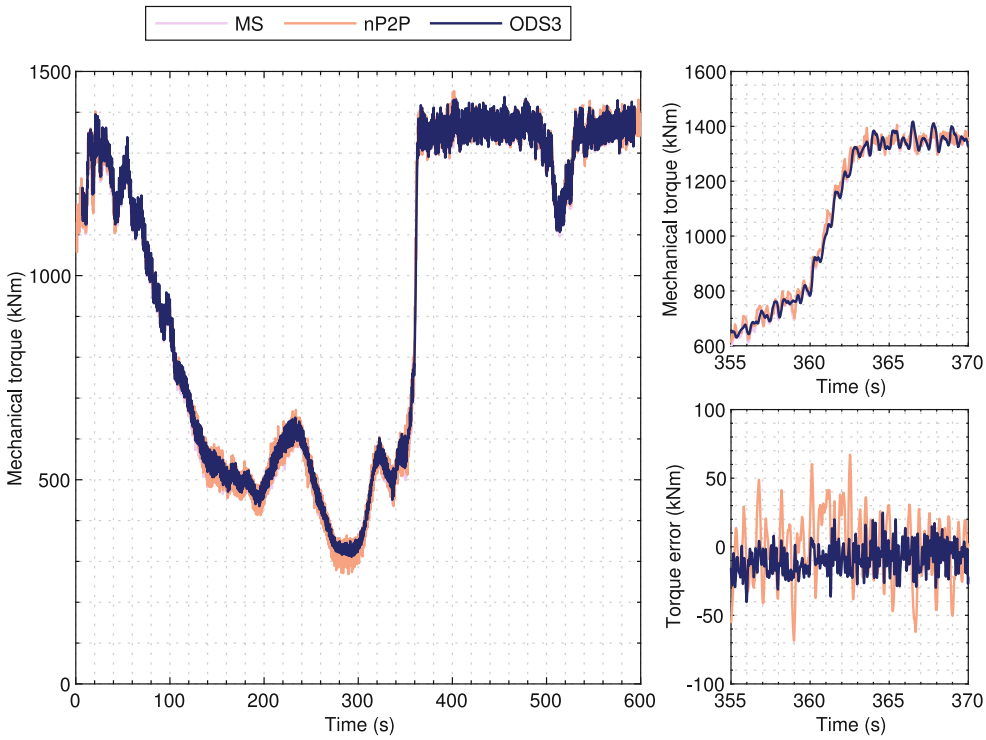


Fig. 12 Comparison of torque measurements derived from fiber-optic and main-shaft strain signals for the example on April 25th at 20:40 UTC

be calibrated to torque because of the *in situ* installation. Instead, the average values of normalized P2P (nP2P) strain and mechanical torque measured by the main-shaft strain gauges for every revolution of the rotor were compared as shown in Fig. 8. A linear relationship is observed with an interpolation coefficient of 9.43 kNm/$\mu\epsilon$. Using this, the nP2P strains can be converted to dynamic mechanical torque for every detected planet passage.

3.2 Operational deflection shape method

This section describes another approach to derive torque from the FOSs based on operational deflection shapes (ODSs). ODSs are similar to natural mode shapes, but because they are caused by periodic external excitations rather than being a structural property of the gearbox, the term ODS is used. In a previous work, [33] described the subspace multivariable output-error state-space (MOESP) algorithm used to identify models from the FOSs and the state reconstruction procedure to quantify the contribution of the ODSs. The contribution of the planet-passing ODSs showed a strong correlation with the dynamic mechanical torque in the gearbox and, therefore, provides a means to estimate torque. The first step of this method is to identify the ODSs from a suitable training dataset at continuously rated operating conditions. The first such conditions occurred on May 5th at 23:00 UTC, in which the turbine was operating at rated speed and power for the entire 10-minute period.

The sampling frequency plays an important role in the efficiency of the numerical implementation of the MOESP algorithm. The original sampling frequency of 2,000 Hz for the FOSs was downsampled to 60 Hz, which matched the sampling frequency of the main-shaft strain gauges. This frequency is still suitable, as it easily captures the 3P planet-passing and gear mesh excitation frequencies for the planetary stage, which at the rated rotor speed of 15.96 rpm (0.266 Hz) are 0.798 Hz and 23.140 Hz, respectively, for the ring gear with 87 teeth and the sun pinion with 18 teeth. Once the sampling frequency has been chosen, three parameters need to be defined to execute the MOESP algorithm [34–36]. These parameters are the number of samples N, the number of block rows s, and the system order n. For the present study, $N = 12,800$ samples per sensor accounting for approximately one-third of the 10-minute data sample, $s = 64$ block rows, and $n = 20$, which is a model order equivalent to 10 oscillatory modes. The observed part of the eigenvectors identified by the MOESP algorithm are the system's mode shapes. The frequency and damping ratios of each ODS, computed from the identified eigenvalues, are listed in Table 1. The damping ratios are all very small, as expected for a stiff, metal structure such as the ring gear, resulting in periodic, undamped dynamic behavior. All identified frequencies match with the 3P planet-passing frequency and its harmonics. Figure 9 shows an animation of the ODSs that correspond to the first three orders of the planet-passing frequency (3P).

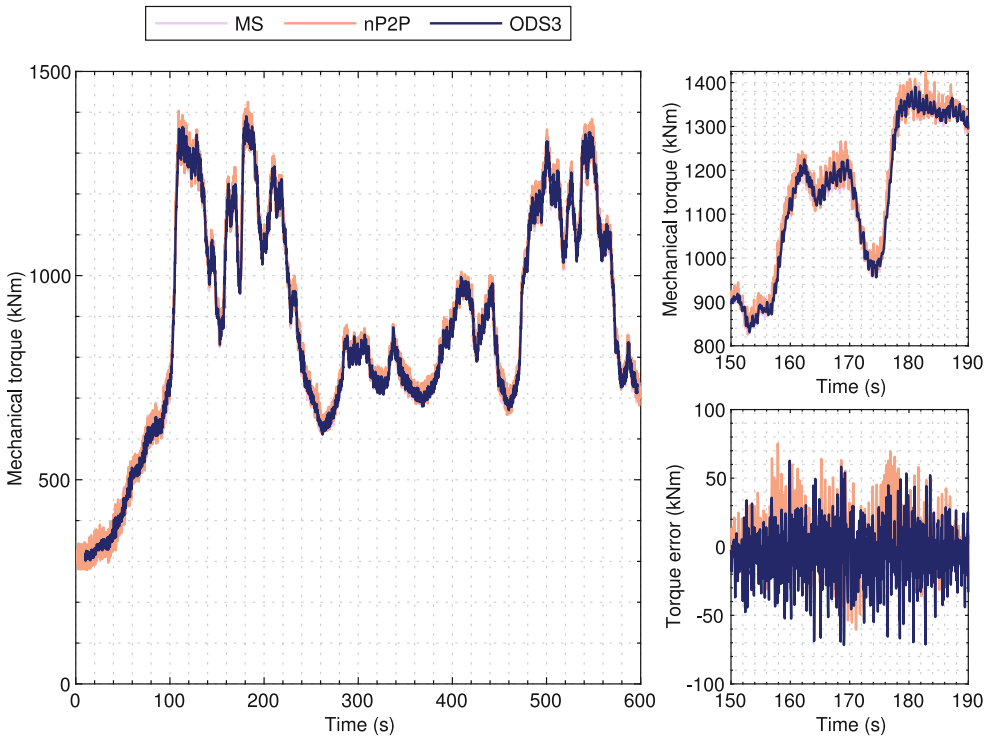


Fig. 13 Comparison of torque measurements derived from fiber-optic and main-shaft strain signals on May 31st at 22:40 UTC

With a suitable transformation matrix, it is possible to diagonalize the identified system matrix $\bar{A}$ into the so-called modal form denoted as $\bar{A}_{\mathrm{M}}$. The same transformation matrix can be used to obtain the output matrix $\bar{C}_{\mathrm{M}}$. The associated states $\hat{x}$ and the output measurements $\hat{y}$ can be reconstructed using the "one-step-ahead" predictor. For this predictor, we use a Kalman gain $\bar{K}_{\mathrm{M}}$ estimated from the measured data as the optimal estimator. The accuracy of the identified system was evaluated using the variance accounted for (VAF) metric between the measured signals y and the predicted $\hat{y}$, representing the strain from the FOSs. The VAF was computed using a different section of the 10-minute training recording used for training, which is the validation dataset. The system's initial state is estimated for the validation part of the dataset using the identified models. Then, the system state and output signals can be reconstructed, assuming the system behaves as an autonomous system oscillating from a nonzero initial condition. An average VAF value for the 23 FOSs of 98.45% was achieved with the above-mentioned identification parameters. Such a high VAF value indicates that the identified ODSs can reproduce the behavior of the gearbox accurately, and the contribution of the periodic excitations accounts for almost all the energy in the measured FOS strain signals.

However, the results were not close to the measured signals when recordings with variable speed were analyzed. For normal operating conditions, where the speed of the turbine is constantly changing, the behavior is no longer periodic in the time domain, so the identified system representation does not hold. To overcome this, the measured strain signals were resampled at fixed angular intervals. In the angular domain, the system exhibits a periodic behavior and can be represented by the ODSs. The strain signals were angularly resampled by using their periodic 3P behavior, previously shown in Fig. 7. The angular resolution was chosen to match the time resolution at rated speed. Figure 10 compares the main-shaft torque, the nP2P strain, and the modules of the dimensionless states associated with each ODS for the example 10-minute recording from April 25th at 20:40 UTC. The trends for the nP2P strain and

Table 2 Normalized RMSE of torque measurements on a time-based approach

Method	RMSE (kNm)			Normalized RMSE (%)		
	Apr 25th 20:40 UTC	May 31st 22:40 UTC	Mean 837 files	Apr 25th 20:40 UTC	May 31st 22:40 UTC	Mean 837 files
nP2P	15.356	16.708	15.768	1.163	1.266	1.195
ODS1	28.434	28.514	20.923	2.154	2.160	1.585
ODS2	20.054	19.057	15.611	1.519	1.444	1.183
ODS3	22.806	18.476	18.015	1.728	1.400	1.365

Table 3 Normalized RMSE of torque measurements based on LRD and LDD approaches

	Average RMSE (kNm)		Average Normalized RMSE (%)	
Method	LRD	LDD	LRD	LDD
nP2P	8.567	8.292	0.649	0.628
ODS1	15.152	13.585	1.148	1.029
ODS2	9.539	8.964	0.723	0.679
ODS3	9.013	8.542	0.683	0.647

the modules for the dimensionless states are the same as the main-shaft torque, giving confidence that both the FOS strain analysis methods and any of the ODSs can be used to measure dynamic mechanical torque. When the system is represented in diagonal form, via a suitable similarity transformation, two conjugate states are associated with each ODS with equal modules.

In order to find the relationship between the module of the states ($\hat{x}$) and the mechanical torque, again, the average values of the state modules and mechanical torque measured by the main-shaft strain gauges for every full revolution of the rotor were determined and are compared as shown in Fig. 11. A linear relationship is observed for every ODS, each with its own interpolation coefficient as listed in the legend. Using these coefficients, the modules of the states can be converted to dynamic mechanical torque for every sample.

4 Results

This section presents the key findings obtained from the field validation campaign. First, we examine the dynamic mechanical torque measurements derived from the FOSs placed on the ring gear and their differences compared to those from the main-shaft strain gauges. Then, we quantify the accuracy of the fiber-optic measurements and analyze the effect of the operating conditions experienced by the turbine throughout the field validation campaign.

4.1 Accuracy assessment

Using the linear interpolation coefficients shown in Fig. 8 and 11, it is possible to convert the nP2P values and ODS state modules into dynamic mechanical torque. In this work, these relationships were defined using average values over a full rotor revolution for the complete measurement campaign. However, for a serial implementation, it is envisaged that the FOSs could be installed during the gearbox assembly and fully calibrated to mechanical torque during the end-of-line gearbox test. For the example 10-minute data recording analyzed in Sect. 3, a comparison between the dynamic mechanical torque measured by the main-shaft strain gauges and the torque measurements derived from the FOS strain signals is shown in Fig. 12. Both the nP2P and third-order (ODS3) torque measurements closely match the dynamic mechanical torque measurements from the main-shaft strain gauges, even in the quick rise in torque from 600 kNm to the rated 1,320 kNm that occurs in only 10 s. The error between the nP2P and ODS torque methods when compared to the main-shaft torque is typically less than 50 kNm, even during this highly dynamic period. Figure 13 shows the dynamic mechanical torque measurements for another 10-minute recording from May 31st at 22:40 UTC. This period features more operation in the variable torque and rotor speed region, with even more changes in torque from as low as 300 kNm to rated for brief periods. In some cases, the torque rises and falls 300 to 400 kNm in as little as 5 s at a time. In this variable-speed region, it does appear, though, that the torque errors increase slightly more but are still typically less than 70 kNm.

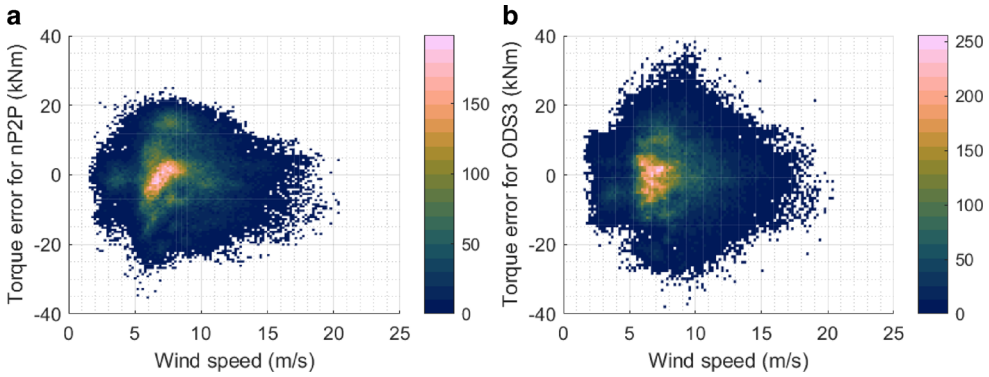


Fig. 14 Effect of wind speed at hub height on the average RMSE for **a** nP2P and **b** ODS3 torque measurement methods for each rotor revolution from April 25th to July 20th

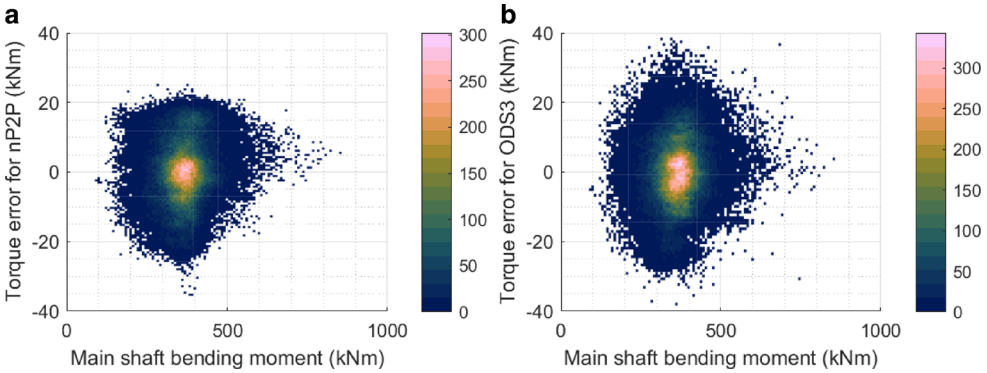


Fig. 15 Effect of main shaft bending moment on the average RMSE for **a** nP2P and **b** ODS3 torque measurement methods for each rotor revolution from April 25th to July 20th

The root-mean-square error (RMSE) was used to assess the accuracy of the dynamic mechanical torque measurements [37]. For every 10-minute recording, such as the examples shown in Figs. 12 and 13, the error was computed as the difference between the dynamic mechanical torque measurements from the main-shaft strain gauges and those derived from FOS magnitudes for each time sample. The main-shaft strain gauge signals were logged with a sampling frequency of 60 Hz. To perform a sample-by-sample computation of the error, the torque measurements obtained using the peak-to-peak method had to be interpolated because a torque value can only be obtained when any of the FBGs detects a planet passage, which generally leads to a nonuniform spacing of the torque samples. In the case of the ODS method, the FOS signals were angularly resampled as explained in Sect. 3.2, and therefore, the main shaft torque was also resampled using the same fixed angular intervals to make the instantaneous error evaluation possible. It is common practice to normalize the RMSE values to assess the magnitude of errors from the perspective of the measured quantity. However, there is no consistent means of normalization in the literature [38]. In this work, the RMSE values were normalized using the rated torque. Table 2 summarizes the normalized RMSE values of the 10-minute recordings from April 25th at 20:40 UTC and May 31st at 22:40 UTC shown in Figs. 12 and 13. The torque RMSE evaluation was also performed for all 837 10-minute recordings from the full validation campaign. These recordings were selected using the minimum produced power requirement of 150 kW. A single normalized RMSE value was obtained from each 10 min, and the average of all 837 values is also shown in Table 2. Depending on the method to derive torque, the RMSE torque errors range from 15 to 30 kNm, which when normalized are approximately 1 to 2.5%. These normalized RMSE values are considered very low, within the expected accuracy of the main shaft strain gauges. Examining just the nP2P and ODS3 methods, the errors are even lower, with normalized errors less than 1.5%. For brevity, in Table 2, only the ODSs corresponding to the first three orders of the planet-passing frequency (ODS1, ODS2, and ODS 3) are shown because the fourth and higher orders resulted in higher errors than the first three.

For fatigue life estimations, because the gears and bearings are subjected to stress cycles even under a constant torque load, the IEC 61400-4 gearbox design standard recommends binning the loads using a load duration distribution approach. The load bins can be the time spent at a given load (i.e., load duration distribution (LDD)) or the number of revolutions (i.e., load revolution distribution (LRD)). The number of gear stress cycles depends on the rotational speed, and therefore, the shaft speed is taken into account in the LDD or LRD. As shown in Sect. 3.1 the rotor or main shaft speed can also be derived from the FOSs. For the 837 analyzed 10-minute recordings, the accuracy of the mechanical torque derived from the FOSs was assessed for

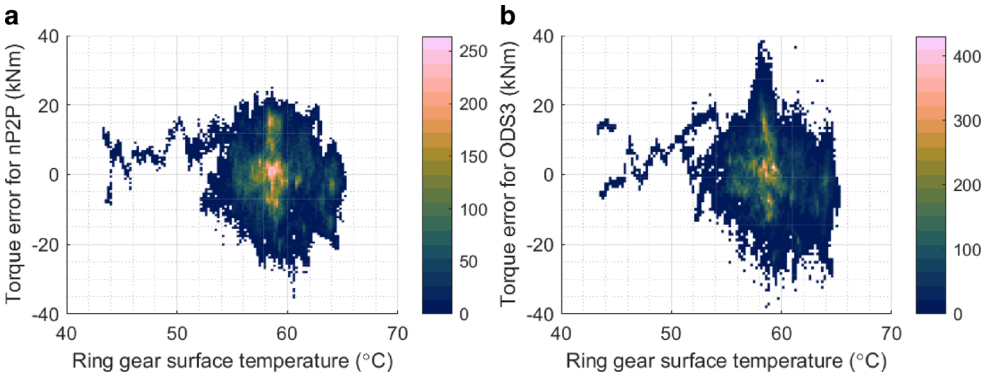


Fig. 16 Effect of ring gear surface temperature on the average RMSE for **a** nP2P and **b** ODS3 torque measurement methods for each rotor revolution from April 25th to July 20th

both LDD and LRD approaches. For the LDD, each 10-minute recording was considered as a time bin, and its average torque value was computed. Similarly, for the LRD, the mechanical torque was averaged for the 113,499 full main-shaft revolutions contained in the 837 files. Table 3 summarizes the overall RMSE in kNm and the normalized RMSE in % for the full measurement campaign using the errors of each 10-minute file and each revolution. As can be seen, the normalized RMSE values drop below 0.7% for both the nP2P and ODS3 methods.

Therefore, these highly accurate results allow the use of dynamic mechanical torque from the FOSs for applications like remaining useful life estimation and potentially even wind turbine control. Although the nP2P method has a similar error as the first 3 ODS methods, the ODS methods have the advantage of a greater sampling frequency. The nP2P method can only provide a torque estimate when a planet passage is detected, in this case at 23×3P per revolution. The ODS method, however, can give a higher sampling frequency because the state associated with the ODSs can be evaluated at every time step and, therefore, can be as high as the sampling frequency. Because it uses simple linear algebraic operations, it can also potentially be implemented in real time. Another advantage of ODS method is that we can recursively implement the system identification algorithm to identify ODS at different times and track the deflection shapes, which could potentially be used for gearbox fault detection. Additionally, the nP2P method encounters difficulty identifying the planet passage peaks at lower torque levels.

4.2 Analysis of effect of wind turbine operational parameters

In this section, the effect of wind turbine operating conditions on the accuracy of the mechanical torque measurements from the FOSs presented in Sect. 4.1 is assessed using the LRD approach. By averaging the torque errors over full revolutions of the rotor and pairing them with the synchronously logged additional wind turbine operating parameters, like wind speed, main-shaft bending moments, and ring gear temperature, it is possible to assess the effect of those operating conditions on the accuracy of the FOSs. Figure 14 shows the error between the mechanical torque measurements from the nP2P and ODS methods and the main-shaft strain gauges across the average wind speed of each LRD bin. The errors are lowest above the rated wind speed of 11 m/s in which the turbine is typically operating at constant rotor speed and mechanical torque, even in wind speeds as high as 21 m/s. The errors are slightly higher in the variable rotor speed region between 6 and 10 m/s, in which the speed, torque, and blade pitch angles are all frequently changing.

Figure 15 shows the error between the mechanical torque measurements from the nP2P and ODS methods and the main-shaft strain gauges across the average main-shaft bending moment of each LRD bin. The majority of the main-shaft bending moments experienced were around 400 kNm, which is close to that caused by the rotor overhung weight moment at the main-shaft bending gauge location described in Sect. 2.2. In many operating conditions, slightly positive and negative wind shear can relieve or add to the main shaft bending moment, respectively, but these moments do not appear to have much effect on the torque error estimate.

One of the concerns when evaluating the accuracy of the FOS measurements was to understand the effect of ring gear temperature on the FBGs. For that purpose, the FOS strains were correlated to the measurements from the ring gear surface temperature sensor described in Sect. 2.2. As Fig. 16 shows, no appreciable correlation was observed between the torque errors and the ring gear temperature for either analysis method over a wide range of ring gear temperatures from 43 to 66 °C. Typical operating temperatures ranged from 50 to 65 °C. From this we can conclude that both the nP2P and the ODS methods are robust to temperature variations.

The effects of other operating variables like wind turbulence intensity, yaw misalignment, and blade pitch angles on the torque error were also found to be negligible, similar to previous analysis of the effect of these parameters on the mesh load factor [31]. This is aligned with the expected behavior of the four-point-mount drivetrain configuration under test described in Sect. 2.

5 Conclusions

Accurate knowledge of the mechanical torque duty cycle of wind turbine gearboxes has become essential in modern designs, as maintaining or even improving gearbox reliability with increasing torque density demands is proving to be challenging. In many wind turbines, the mechanical torque is estimated from the generator electrical operational parameters; however, there are inherent uncertainties in the gearbox and electrical system efficiencies that vary with load, temperature, and time. Further, the electrical torque is zero in transient conditions, but highly dynamic mechanical torque is still present. Direct measurement of mechanical torque in the rotating system can be accomplished but can be costly.

In this work, a cost-effective method of measuring the dynamic mechanical torque based on fiber-optic strain sensors placed on the outer surface of the gearbox ring gear of a Gamesa G97 2 MW wind turbine was validated over a 3-month field test campaign. The fiber optic sensors measure

the radial deformation of the ring gear, which is proportionate to the mechanical torque. The dynamic mechanical torque derived from the fiber optic strain sensors were compared to torque derived from traditional strain gauges installed on the main shaft with an average normalized root-mean-square error of less than 0.7% using the load revolution distribution analysis. The effect of operating conditions on the torque estimate was also investigated, without an appreciable or consistent influence from wind speed, main-shaft bending moment, or ring gear temperature. The method based on the third planet-passing operational deflection shape has several advantages over the peak-to-peak method, such as a higher sampling frequency and potential for real-time application, and therefore is the preferred method. The fiber-optic strain sensors' successful operation during the complete test campaign demonstrated a robust and accurate solution for fleet-wide enhanced gearbox remaining useful life estimation that has been increased to a technology readiness level of 7 as defined in ISO 16290.

Acknowledgements The authors wish to acknowledge financial support from Siemens Gamesa Renewable Energy and Sensing360 that made it possible to conduct the present study. This work was also authored in part by the National Renewable Energy Laboratory operated by the Alliance for Sustainable Energy, LLC, for the U.S. Department of Energy (DOE) under contract no. DEAC36-08GO28308. Funding was provided by the U.S. Department of Energy Office of Energy Efficiency and Renewable Energy Wind Energy Technologies Office. The views expressed in the article do not necessarily represent the views of the DOE or the U.S. Government. The U.S. Government retains and the publisher, by accepting the article for publication, acknowledges that the U.S. Government retains a nonexclusive, paid-up, irrevocable, worldwide license to publish or reproduce the published form of this work, or allow others to do so, for U.S. Government purposes. The authors would also like to thank our NREL colleagues Jerry Hur, Brian Manoa, and Anna McAuliffe for their support during the sensor installation, and Jason Roadman and Scott Dana during the data acquisition process.

Conflict of interest U. Gutierrez-Santiago, J. Keller, A. Fernández-Sisón, H. Polinder and J.-W. van Wingerden declare that they have no competing interests.

Open Access Dieser Artikel wird unter der Creative Commons Namensnennung 4.0 International Lizenz veröffentlicht, welche die Nutzung, Vervielfältigung, Bearbeitung, Verbreitung und Wiedergabe in jeglichem Medium und Format erlaubt, sofern Sie den/die ursprünglichen Autor(en) und die Quelle ordnungsgemäß nennen, einen Link zur Creative Commons Lizenz beifügen und angeben, ob Änderungen vorgenommen wurden. Die in diesem Artikel enthaltenen Bilder und sonstiges Drittmaterial unterliegen ebenfalls der genannten Creative Commons Lizenz, sofern sich aus der Abbildungslegende nichts anderes ergibt. Sofern das betreffende Material nicht unter der genannten Creative Commons Lizenz steht und die betreffende Handlung nicht nach gesetzlichen Vorschriften erlaubt ist, ist für die oben aufgeführten Weiterverwendungen des Materials die Einwilligung des jeweiligen Rechteinhabers einzuholen. Weitere Details zur Lizenz entnehmen Sie bitte der Lizenzinformation auf http://creativecommons.org/licenses/by/4.0/deed.de.

References

1. Veers P, Dykes K, Lantz E, Barth S, Bottasso CL, Carlson O, Clifton A, Green J, Green P, Holttinen H, Laird D, Lehtomäki V, Lundquist JK, Manwell J, Marquis M, Meneveau C, Moriarty P, Munduate X, Muskulus M, Naughton J, Pao L, Paquette J, Peinke J, Robertson A, Rodrigo JS, Sempreviva AM, Smith JC, Tuohy A, Wiser R (2019) Grand challenges in the science of wind energy. Science 366(6464):2027. https://doi.org/10.1126/science.aau2027
2. Nejad AR, Keller J, Guo Y, Sheng S, Polinder H, Watson S, Dong J, Qin Z, Ebrahimi A, Schelenz R, Gutiérrez Guzmán F, Cornel D, Golafshan R, Jacobs G, Blockmans B, Bosmans J, Pluymers B, Carroll J, Koukoura S, Hart E, McDonald A, Natarajan A, Torsvik J, Moghadam FK, Daems P-J, Verstraeten T, Peeters C, Helsen J (2022) Wind turbine drivetrains: state-of-the-art technologies and future development trends. Wind Energy Sci 7(1):387–411. https://doi.org/10.5194/wes-7-387-2022
3. Stehly T, Duffy P, Mulas HD (2023) 2022 cost of wind energy review. Technical report NREL/PR-5000-88335. Natl Renew Energy Lab. https://doi.org/10.2172/2278805
4. Carroll J, McDonald A, McMillan D (2016) Failure rate, repair time and unscheduled O&M cost analysis of offshore wind turbines. Wind Energy 19(6):1107–1119. https://doi.org/10.1002/we.1887
5. Santelo TN, de Oliveira CMR, Maciel CD, de Monteiro BAJR (2022) Wind turbine failures review and trends. J Control Autom Electr Syst 33(2):505–521. https://doi.org/10.1007/s40313-021-00789-8
6. Veers P, Bottasso CL, Manuel L, Naughton J, Pao L, Paquette J, Robertson A, Robinson M, Ananthan S, Barlas T, Bianchini A, Bredmose H, Horcas SG, Keller J, Madsen HA, Manwell J, Moriarty P, Nolet S, Rinker J (2023) Grand challenges in the design, manufacture, and operation of future wind turbine systems. Wind Energy Sci 8(7):1071–1131. https://doi.org/10.5194/wes-8-1071-2023
7. Lantz E (2013) Operations expenditures: historical trends and continuing challenges. Technical report NREL/PR-6A20-58606. Natl Renew Energy Lab. https://www.nrel.gov/docs/fy13osti/58606.pdf
8. Pulikollu RV (2023) Wind turbine reliability benchmarking to reduce O&M costs. https://app.box.com/s/xti5nxixt4uwz2wtobqcvt7t1hgnmkb7
9. Haus L, Sheng S, Pulikollu RV (2024) Wind turbine major systems reliability trends and mitigation strategies. https://app.box.com/s/ktjzjdxn77omu1cjoy9znymbrynlsw0d
10. Keller J, Guo Y, Zhang Z, Lucas D (2018) Comparison of planetary bearing load-sharing characteristics in wind turbine gearboxes. Wind Energy Sci 3(2):947–960. https://doi.org/10.5194/wes-3-947-2018
11. Keller J (2021) Gearbox reliability collaborative 1.5 (GRC1.5) project: joint industry megawatt scale gearbox field tests. Technical report NREL/TP-5000-81064. Natl Renew Energy Lab. https://doi.org/10.2172/1822382
12. Keller J (2024) GRC1.5 project: joint industry megawatt scale gearbox field tests. Technical report NREL/TP-5000-88867. Natl Renew Energy Lab. https://doi.org/10.2172/2311139
13. Demas NG, Lorenzo-Martin C, Luna R, Erck RA, Greco AC (2023) The effect of current and lambda on white-etch-crack failures. Tribol Int 189:108951. https://doi.org/10.1016/j.triboint.2023.108951
14. Dykes KL, Veers PS, Lantz EJ, Holttinen H, Carlson O, Tuohy A, Sempreviva AM, Clifton A, Rodrigo JS, Berry DS, Laird D, Carron WS, Moriarty PJ, Marquis M, Meneveau C, Peinke J, Paquette J, Johnson N, Pao L, Fleming PA, Bottasso C, Lehtomaki V, Robertson AN, Muskulus M, Manwell J, Tande JO, Sethuraman L, Roberts JO, Fields MJ (2019) IEA wind TCP: results of IEA wind TCP workshop on a grand vision for wind energy technology. Tech-

nical report NREL/TP-5000-72437. Int Energy Agency. https://doi.org/10.2172/1508509
15. Helsen J, Guo Y, Keller J, Guillaume P (2016) Experimental investigation of bearing slip in a wind turbine gearbox during a transient grid loss event. Wind Energy 19(12):2255–2269. https://doi.org/10.1002/we.1979
16. Egeling T, Hidding E, Hövelbrinks DN, Endemann Uhlending M, Bonnet RP, Dekkers HW, Vandermeulen W (2018) Digital gearbox use case. https://www.winergy-group.com/en/DigitalGearboxUseCase. Accessed 24 Nov 2021
17. Röder J, Jacobs G, Duda T, Bosse D, Herzog F (2021) Investigation of dynamic loads in wind turbine drive trains due to grid and power converter faults. Energies. https://doi.org/10.3390/en14248542
18. Santos R, van Dam J (2015) Mechanical loads test report for the U.S. Department of energy 1.5-megawatt wind turbine. Technical report NREL/TP-5000-63679. Natl Renew Energy Lab. https://doi.org/10.2172/1215119
19. Rosinski J, Smurthwaite D (2010) Troubleshooting wind gearbox problems. Gear solutions, pp 22–33
20. Perišić N, Kirkegaard PH, Pedersen BJ (2015) Cost-effective shaft torque observer for condition monitoring of wind turbines. Wind Energy 18(1):1–19. https://doi.org/10.1002/we.1678
21. Azzam B, Baseer A, Schelenz R, Jacobs G (2021) Development of a wind turbine gearbox virtual sensor using multibody simulation and artificial neural networks. Forsch Ingenieurwes 85:241–250. https://doi.org/10.1007/s10010-021-00460-3
22. Cappelle C, Cattebeke M, Bosmans J, Kirchner M, Croes J, Desmet W (2021) Sensor selection for cost-effective virtual torque measurements on a wind turbine gearbox. Forsch Ingenieurwes 85:325–334. https://doi.org/10.1007/s10010-021-00464-z
23. Mehlan F, Keller J, Nejad RA (2023) Virtual sensing of wind turbine hub loads and drivetrain fatigue damage. Forsch Ingenieurwes 87:207–218. https://doi.org/10.1007/s10010-023-00627-0
24. Mora B, Basurko J, Sabahi I, Leturiondo U, Albizuri J (2023) Strain virtual sensing for structural health monitoring under variable loads. Sensors. https://doi.org/10.3390/s23104706
25. Bosmans J, Kirchner M, Croes J, Desmet W (2023) Validation of a wind turbine gearbox strain simulation model in service to virtual testing. Forsch Ingenieurwes 87:107–117. https://doi.org/10.1007/s10010-023-00635-0
26. Bosmans J, Gallas S, Smeets V, Kirchner M, Geens L, Croes J, Desmet W (2025) Experimental validation of virtual torque sensing for wind turbine gearboxes based on strain measurements. Wind Energy 28(2). https://doi.org/10.1002/we.2955
27. Glavind L, Olesen I, Skipper B, Kristensen M (2013) Fiber-optical grating sensors for wind turbine blades: a review. Opt Eng 52(3):1–10. https://doi.org/10.1117/1.OE.52.3.030901
28. Kreuzer M (2006) Strain measurement with fiber bragg grating sensors. HBM
29. Gutierrez-Santiago U, Fernández Sisón A, Polinder H, Wingerden J-W (2022) Input torque measurements for wind turbine gearboxes using fiber-optic strain sensors. Wind Energy Sci 7(2):505–521. https://doi.org/10.5194/wes-7-505-2022
30. Siddiqui MO, Feja PR, Borowski P, Kyling H, Nejad AR, Wenske J (2023) Wind turbine nacelle testing: state-of-the-art and development trends. Renew Sustain Energy Rev. https://doi.org/10.1016/j.rser.2023.113767
31. Gutierrez-Santiago U, Keller J, Fernández Sisón A, Polinder H, Wingerden J-W (2024) Instantaneous mesh load factor (K_γ) measurements in a wind turbine gearbox using fiber-optic strain sensors. J Phys: Conf Ser 2767:42022. https://doi.org/10.1088/1742-6596/2767/4/042022
32. Riccobono N, Danigelis N, Keller J, Gutierrez-Santiago U (2025) Main shaft bending moment analysis for a Gamesa G97 2-MW wind turbine. Technical report NREL/TP-5000-91332, Natl Renew Energy Lab. https://www.nrel.gov/docs/fy25osti/91332.pdf
33. Gutierrez Santiago U, Vondelen A, Fernández Sisón A, Polinder H, Wingerden J-W (2025) Identification of operational deflection shapes of a wind turbine gearbox using fiber-optic strain sensors on a serial production end-of-line test bench. Wind Energy Sci 10(1):207–225. https://doi.org/10.5194/wes-2024-83
34. Verhaegen M, Verdult V (2007) Filtering and system identification: a least squares apporach. Cambridge University Press, Cambridge https://doi.org/10.1017/CBO9780511618888
35. Verhaegen M, Verdult V, Bergboer N (2007) Filtering and system identification: an introduction to using matlab software, 1 august 2007 edn. Delft University of Technology, Delft, The Netherlands (https://www.dcsc.tudelft.nl/~jwvanwingerden/lti/doc/companion.pdf)
36. Houtzager I (2012) LTI system identification toolbox (https://www.dcsc.tudelft.nl/~jwvanwingerden/lti/ltitoolbox_product_page.htm)
37. Chai T, Draxler RR (2014) Root mean square error (RMSE) or mean absolute error (MAE)?—arguments against avoiding RMSE in the literature. Geosci Model Dev 7(3):1247–1250. https://doi.org/10.5194/gmd-7-1247-2014
38. Krause A, Jacobs G, Röder J, Zweiffel M, Roth J (2024) Deviation of drive torque and rotational speed of a wind turbine drivetrain between test bench and wind turbine simulations. J Phys: Conf Ser 2767(4):42013. https://doi.org/10.1088/1742-6596/2767/4/042013

Publisher's Note Springer Nature remains neutral with regard to jurisdictional claims in published maps and institutional affiliations.